RESEARCH ARTICLE | JULY 16 2025

Enhancing vibration isolation and energy harvesting via a quasi-zero stiffness electromagnetic system

Junlei Wang ; Han Li; Daniil Yurchenko ; Haigang Tian ; Guobiao Hu

Appl. Phys. Lett. 127, 023904 (2025)
https://doi.org/10.1063/5.0274334

Applied Physics Letters ARTICLE pubs.aip.org/aip/apl

Enhancing vibration isolation and energy harvesting via a quasi-zero stiffness electromagnetic system

Cite as: Appl. Phys. Lett. **127**, 023904 (2025); doi: 10.1063/5.0274334
Submitted: 5 April 2025 · Accepted: 27 June 2025 ·
Published Online: 16 July 2025

Junlei Wang,[1] Han Li,[1] Daniil Yurchenko,[2] Haigang Tian,[1,a)] and Guobiao Hu[3,a)]

AFFILIATIONS

[1]School of Mechanical and Power Engineering, Zhengzhou University, Zhengzhou 450001, China
[2]Institute of Sound and Vibration Research, University of Southampton, SO17 1BJ, United Kingdom
[3]Thrust of Internet of Things, The Hong Kong University of Science and Technology (Guangzhou), Guangzhou, Guangdong 511400, China

[a)]**Authors to whom correspondence should be addressed:** tianhaigang@zzu.edu.cn and guobiaohu@hkust-gz.edu.cn

ABSTRACT

Vibration-related issues are common causes of failure in precision machines, and energy harvesting techniques can help mitigate harmful vibrations and recycle waste energy. This Letter introduces an electromagnetic energy harvester utilizing a quasi-zero stiffness mechanism to achieve simultaneous vibration isolation and energy harvesting. The system utilizes mutually exclusive magnets to generate positive stiffness and flexible bending beams to offer negative stiffness, which counterbalances each other to realize quasi-zero stiffness. Physical prototypes were fabricated, and their vibration isolation and energy harvesting performance were assessed under various magnet distances and excitation conditions. Experimental results validate that the proposed system achieves both vibration isolation and energy harvesting. It exhibits outstanding vibration isolation performance when the frequency exceeds 5 Hz. Notably, the magnet distance significantly affects the energy harvesting performance: compared to the 37 mm configuration, adjusting the magnet distance to 41 and 39 mm increased the power output by 54.9% and 31.7%, respectively. This study lays an important foundation for advancing integrated vibration isolation and energy harvesting technologies.

Vibration exists extensively in the natural environment, and vibration induced issues often lead to the failure of precision machinery.[1–3] As a result, significant efforts have been dedicated to mitigate and suppress harmful vibrations. Depending on the mechanism, vibration isolation techniques are typically categorized as passive,[4–7] semi-active,[8–11] and active.[12–14] However, adopting vibrational energy harvesting techniques can convert harmful vibrational energy into useful electrical energy. Common energy conversion mechanisms include piezoelectric,[15–18] electromagnetic,[19–21] and triboelectric.[22–25] In recent years, quasi-zero stiffness (QZS) vibration energy harvesting has attracted significant research interest[26–32] for its ability to passively suppress low and ultralow-frequency vibrations and simultaneously harvest low-frequency energy.

By leveraging the QZS mechanism, Li and Jing[33] proposed a bistable electromagnetic energy harvester specifically for wave energy harvesting. They demonstrated that its efficiency was significantly improved compared to the linear one. Inspired by the dynamic coupling in bird limbs and tails, Fang *et al.*[34] designed an energy harvester that integrates an X-shaped QZS isolator. Sui *et al.*[35] developed a QZS vibration isolation piezoelectric energy harvester with four flexure beams and one spring. They validated its ability to isolate low-frequency vibrations and achieve a power output of 3.191 mW at an excitation displacement of 2.5 mm and a pre-stress of 66 N.

Most existing studies on QZS mechanism design focus on negative stiffness and its integration with linear springs. Yan *et al.*[36] utilized linear springs and mutually exclusive magnets as positive stiffness elements to counterbalance negative stiffness, achieving QZS with significantly smaller deformations. However, the paper did not measure the vibration isolation effect of the vibration isolator by shaking table experiments. In addition, there existed fewer studies on the vibration isolation and energy harvesting characteristics by using nonlinear positive stiffness. To address this gap, it is crucial to investigate the vibration isolation and energy harvesting performance based on QZS mechanisms built on nonlinear positive stiffness. Such exploration not

only deepens our understanding of nonlinear QZS dynamics but also highlights their practical value in real-world applications. Such QZS-based electromagnetic systems are well-suited for applications in precision machinery (e.g., semiconductor equipment) requiring low-frequency vibration isolation, as well as in self-powered sensors for structural health monitoring, enabling sustainable wireless sensing without the need for external power sources.

To achieve simultaneous vibration isolation and energy harvesting, an electromagnetic energy harvester system based on QZS is proposed, as shown in Fig. 1(a). The system employs a support platform, three flexible beams, a guide rod, a pair of repulsive magnets, a base, a sleeve, and a coil. In this study, the cylindrical magnets are axially magnetized, with magnetic poles located on their flat circular faces. This configuration directs the magnetic field lines along the central axis, ensuring strong axial flux linkage with the surrounding coil. The axial alignment enhances electromagnetic induction efficiency by maximizing the magnetic flux variation during relative motion, in accordance with Faraday's law. The coupling effect of positive and negative stiffness could produce the QZS characteristics at an appropriate magnet distance. The coil is positioned outside the sleeve and fixed to the base, aiming to harvest energy. Therefore, the system is capable of achieving both vibration isolation and energy harvesting functions. Table I lists the specific parameters of the harvester.

Figures 1(b) and 1(c) show the experimental setup for testing. In the experiment, a shaker (VT-500) is used to generate sinusoidal excitation. The prototype is mounted on the shaker. The sinusoidal excitation with dual-target control of acceleration and displacement is applied to the shaker. The initial condition is set to 5 Hz with an excitation displacement of 2 mm, while the target condition is set to 20 Hz with an excitation acceleration of 3 g. Two accelerometers are fixed at the bottom and top of the prototype to measure the input and output accelerations, respectively. These accelerations are recorded at 0.5 Hz intervals in the range of 5–20 Hz. The acquired data are used to analyze the vibration isolation performance of the system. An external resistor box is connected to the coil, and the voltage across the resistor is measured using a NI data acquisition card (NI-9229).

From a theoretical perspective, the equivalent magnetic charge model can be used to calculate the axial repulsion force between the two permanent magnets. Assuming both magnets are uniformly magnetized along the axial direction (denoted by the unit vector e_z) with magnetization $\mathbf{M} = M\, e_z$, the corresponding surface magnetic charge densities are given by

$$\sigma_m = \pm M.$$

Let PM^a and PM^b be two identical magnets with radius R, height h, and an axial center-to-center separation distance d. The total magnetic force between them results from four pairwise Coulomb-type interactions between their magnetic surface charges. The total force can be expressed as

$$\boldsymbol{F}_{PM^a,PM^b} = \frac{\mu_0 M^2}{4\pi} \sum_{k=1}^{2} \sum_{k'=1}^{2} (-1)^{k+k'} \iint_{S_k} \iint_{S_{k'}} \frac{\boldsymbol{r}_k - \boldsymbol{r}_{k'}}{|\boldsymbol{r}_k - \boldsymbol{r}_{k'}|^3} dS_k dS_{k'}.$$

In this expression, μ_0 denotes the magnetic permeability of free space, and M is the magnitude of the magnetization vector. S_k and $S_{k'}$ represent the circular top ($k = 1$) and bottom ($k = 2$) faces of magnets PM^a and PM^b, respectively. The factor $(-1)^{k+k'}$ accounts for the sign of the surface charges on each face. Surface integrals are evaluated in cylindrical coordinates. Each surface element's position vector is defined as

$$r_{k'} = \begin{bmatrix} r' \cos \phi' \\ r' \sin \phi' \\ z_{k'} \end{bmatrix}, \quad r_k = \begin{bmatrix} r \cos \phi \\ r \sin \phi \\ z_k \end{bmatrix},$$

where $r, r' \in [0, R]$ are radial coordinates of integration; $\varphi, \varphi' \in [0, 2\pi]$ are angular coordinates; $z_k \in \{0, h\}$ are vertical positions of PMa's surfaces; and $z_k' \in \{d, d+h\}$ are vertical positions of PM^b's surfaces.

The negative stiffness of the flexible beams is evaluated through a combination of theoretical modeling and numerical calculations based on the large-deflection beam theory.[35] Each flexible beam undergoes significant geometric nonlinearity due to axial compression, resulting in a non-monotonic force–displacement relationship. The total restoring force in the vertical direction is obtained by summing the vertical components of the axial forces from all three symmetrically arranged beams.

The restoring force can be expressed as

$$F_z(z) = 3 \cdot \left(\frac{dU_b}{d\Delta x} \right) \cdot \frac{L}{\sqrt{L^2 + z^2}},$$

where U_b is the total strain energy of a single beam under large deformation, L is the radial distance from beam base to platform center at equilibrium, z is the vertical displacement of the platform, and Δx is the axial compression, which varies with z and is defined as

FIG. 1. The electromagnetic energy harvester system: (a) schematic diagram, (b) and (c) experimental setup.

TABLE I. The structural parameters of the system.

Description	Parameters	Values
Flexible beam	Length (L_b) × Width (W_b) × Thickness (H_b)	$115 \times 20 \times 0.6\,\text{mm}^3$
Magnet (N52)	Diameter (D_m) × Thickness (H_m)	$20 \times 5\,\text{mm}^2$
Coil (6.8 Ω)	Inside diameter (D_{ci}) × Height (H_c) × Wire diameter (D_{cw}) × Turns (N)	24 mm × 25 mm × 0.45 mm × 580

$$\Delta x(z) = L_b - \sqrt{L^2 + z^2}.$$

L_b is the original length of the beam, and U_b can be expressed as

$$U(\Delta x) = \int_0^{L_b} \frac{1}{2} EI \left(\frac{d^2 w}{dx^2}\right)^2 dx,$$

where EI is the flexural rigidity, and $w(x)$ is the transverse deflection of the beam. The axial restoring force of a single beam can then be calculated as the derivative $\frac{dU_b}{d\Delta x}$, and its vertical component is obtained by projecting this force onto the vertical axis. The total vertical restoring force is then determined by summing the vertical components from all three beams.

The nonlinear repulsive force generated by a pair of mutually repelling magnets[36] enables multiple zero stiffness points within the QZS range. Experiments are designed to investigate the effects of different magnet distances on the QZS characteristics. The harvester is subjected to statics tests using a tensiometer to measure the reaction force vs displacement curves, and the results are shown in Fig. 2. The green curve represents the dynamic stiffness characteristics of the harvester. Varying the initial magnets distance to 37, 39, and 41 mm, the harvester demonstrates excellent QZS characteristics. The corresponding pre-stress conditions also change, and the zero stiffness points for the three configurations are 4.50, 4.00, and 3.35 N, respectively.

The displacement transfer rate is a key index for evaluating the vibration isolation performance of the harvester system. It is defined as the ratio of the absolute displacement y_2 of the load to the excitation displacement y_1 of the base. In the experiment, two accelerometers are used simultaneously to measure the absolute acceleration of the load a_2 and the excitation acceleration of the base a_1. Adopting the acceleration values evaluates the isolation performance in this Letter. The transmission can be calculated by the equation $T = 20lg(a_2/a_1)$. When T=0,

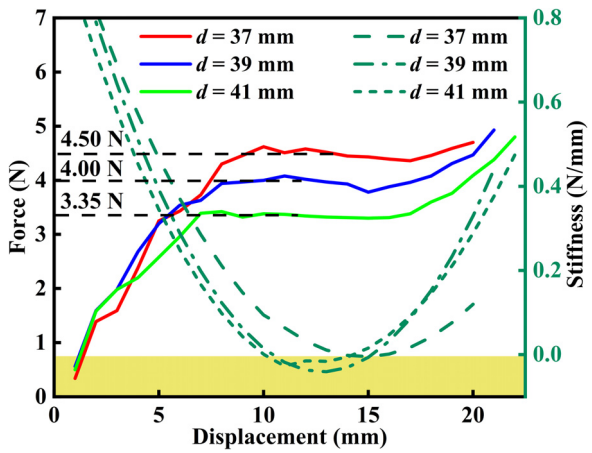

FIG. 2. QZS characteristics at different magnet distances.

meaning the output displacement amplitude exactly equals the input displacement amplitude, the harvester reaches the critical condition, and the corresponding frequency is denoted as f_{critical}. When $T < 0$, vibration isolation occurs. Specifically, when $T = -20$, indicating that the output displacement of the prototype is only one-tenth of the input displacement, the corresponding frequency is referred to as $f_{-20\text{dB}}$.

Figure 3(a) illustrates the displacement transfer rate curves vs frequency at different magnet distances. It can be observed that the f_{critical} point of the prototype is below 5 Hz under the three magnet distances of 37, 39, and 41 mm, and the $f_{-20\text{dB}}$ point falls within the range of 10–12 Hz. Additionally, the displacement transmission decreases with increasing frequency, which demonstrates the excellent vibration isolation performance of the designed system.

Figure 3(b) illustrates the input and output acceleration time-domain curves at frequencies of 9, 12, and 16 Hz. By analyzing the sinusoidal peaks, it is evident that the vibration isolation effect is similar at 9, 12, and 16 Hz for $d = 37$ and $d = 39$ mm. However, for $d = 41$ mm, the vibration isolation effect is superior to the others. It is important to note that the output acceleration curve in Fig. 3(b) is not a perfectly sinusoidal waveform. This is because the sleeve and the magnet have lateral perturbation and friction damping, and the experimental disturbance affects uniform counterweights.

In the design of the electromagnetic harvester, the air gap between the coil and the magnet plays a critical role in determining the magnetic flux linkage, and thus affecting the output performance. Although the current study does not focus on air gap optimization, prior work[37] has shown that reducing the air gap enhances the magnetic flux density intersecting the coil, thereby increasing the induced voltage. Based on this understanding, the coil's inner diameter was minimized as much as practical to reduce the air gap while ensuring mechanical stability. Further optimization and sensitivity analysis of the air gap will be considered in future work.

Due to the QZS characteristics of the harvester, the vibration of the magnet connected to the guide bar differs from that of the coil, allowing the coil to cut the magnetic field and generate electrical energy. This offers the possibility of achieving simultaneously vibration isolation and energy harvesting. Therefore, studies are conducted to explore the energy harvesting characteristics of the harvester. The impedance matching on the harvester is first performed. With an excitation frequency of 15 Hz and an excitation acceleration of 1.4 g, the external resistance is varied, and the corresponding voltage is recorded and processed to determine the power output. The resistance (7 Ω) that maximized the output power is identified as the optimal resistance and selected for subsequent tests. Given that the minimum step increment of the resistor box used in the experiment is 1 Ω, this result closely aligns with the internal resistance of the coil (6.8 Ω).

Figure 4 illustrates the curves of output voltage and power vs the excitation frequency. Both the output voltage and power increase with the increase in the excitation frequency. This trend is consistent with

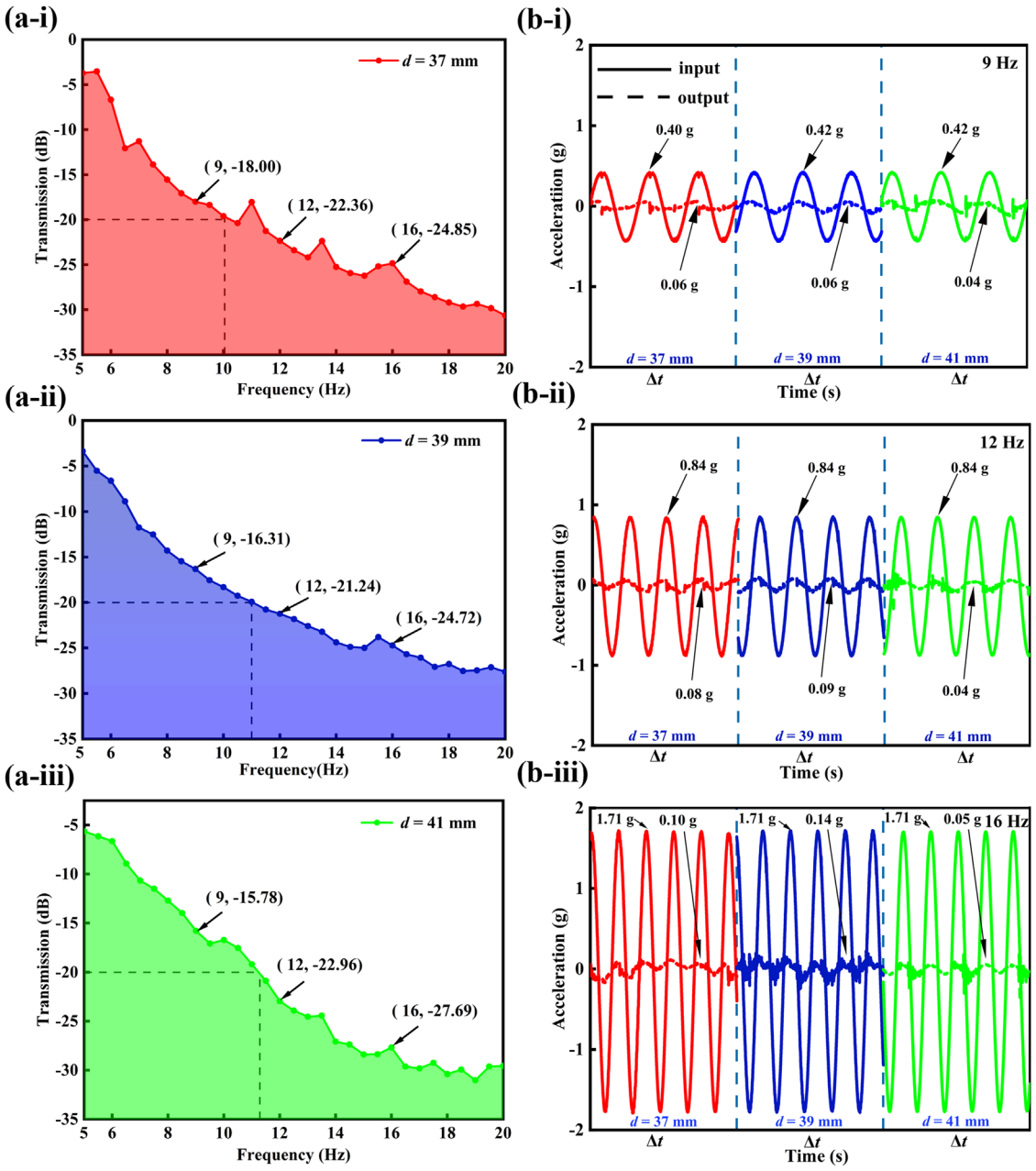

FIG. 3. The vibration isolation performance of the harvester: (a) displacement transmission at 37, 39, and 41 mm, and (b) input and output accelerations at 9, 12, and 16 Hz.

the vibration isolation performance: when the vibration isolation improves, the energy harvesting efficiency of the harvester also increases. This is partly because, as the excitation frequency increases, the excitation acceleration also rises, accelerating the coil's motion relative to the magnetic field and thus increasing the output voltage. Additionally, since the coil moves in synchronization with the base vibration, better vibration isolation results in smaller vibrations of the upper magnet relative to the base, increasing the relative speed between the coil and magnet and thus improving the output voltage.

Figure 4(b) shows that different initial magnet distances also affect the energy harvesting performance of the harvester. At an excitation frequency of 20 Hz, the output power of the harvester with $d = 39$ and $d = 41$ mm is 2.824 and 3.322 mW, respectively, which increased 31.7% and 54.9% compared to the 2.144 mW at 37 mm, respectively. In addition, the subfigures illustrate the time-range curves of the swept output voltage for the three operating conditions. The parameters for this sweep experiment are consistent with the dual-target control settings for excitation acceleration and excitation displacement.

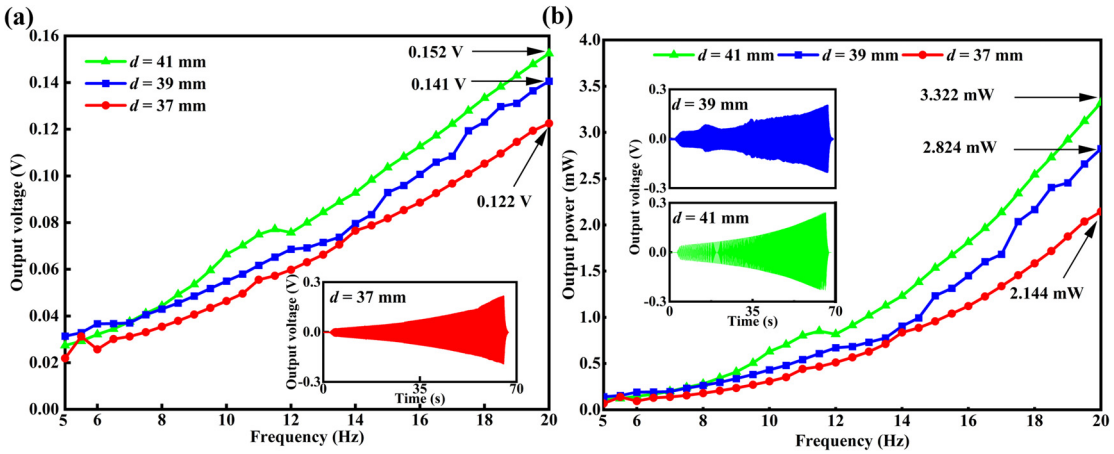

FIG. 4. The energy harvesting performance of harvester. (a) Output voltage and (b) Output power.

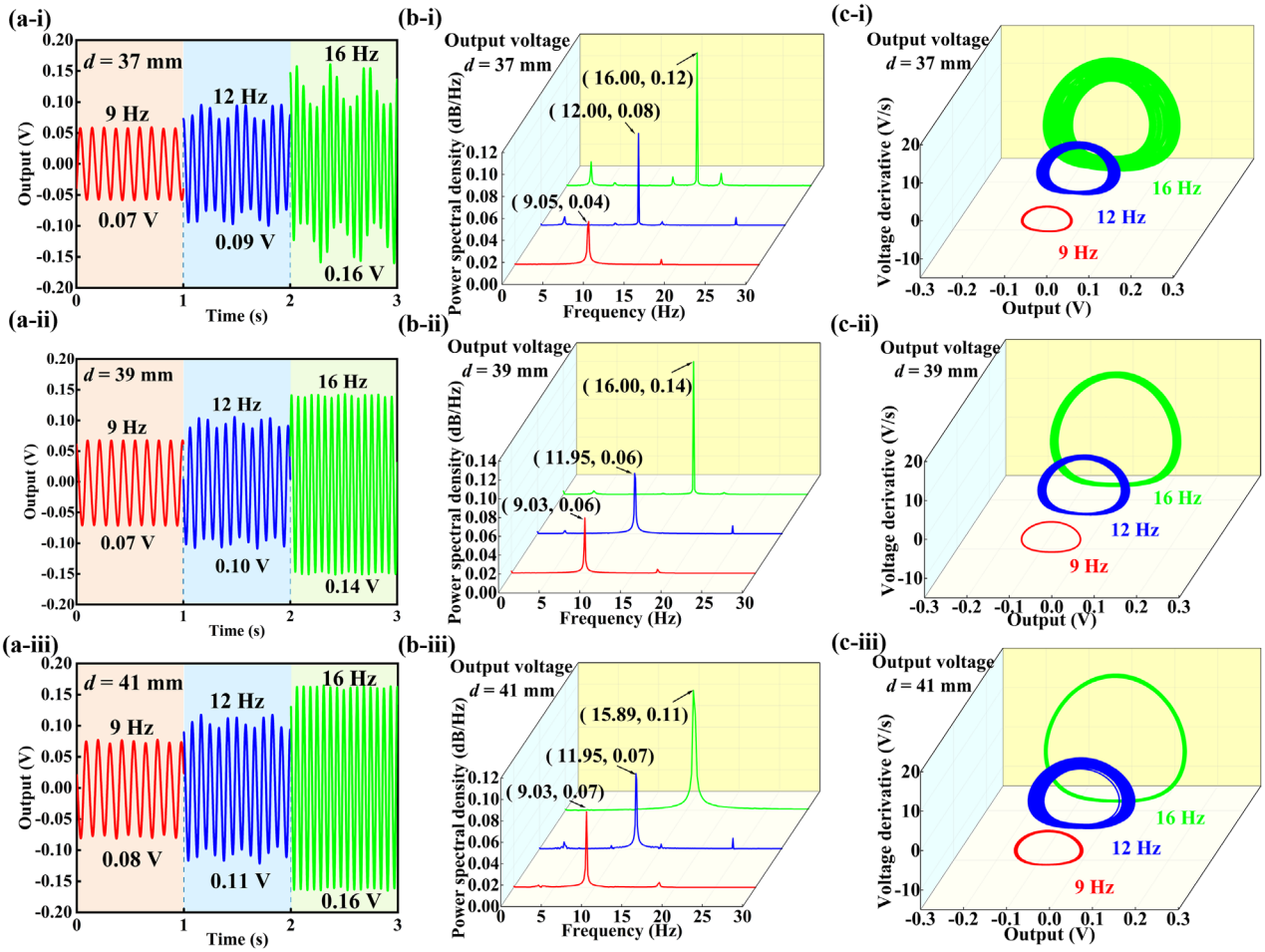

FIG. 5. The energy harvesting performance at 37, 39, and 41 mm: (a) time history, (b) FFT analyses, and (c) phase diagram.

Figure 5(a) illustrates the time-domain output voltage under the excitation frequencies of 9, 12, and 16 Hz. Increasing the excitation frequency, the vibration amplitude correspondingly increases. The voltage–time curves are further analyzed using the Fast Fourier Transform (FFT), as shown in Fig. 5(b). It can be observed that the vibration frequency closely matches the input excitation frequency. This is because the output acceleration, after vibration isolation, is significantly smaller than the input acceleration. Figure 5(c) presents the phase diagram at different excitation frequencies. The phase diagram reveals that the prototype operates in a limiting cyclic oscillation (LCO). This indicates that the harvester does not settle to a stop over time but instead stabilizes into a steady cyclic oscillation.

This Letter presented a multifunctional device incorporating a quasi-zero stiffness mechanism and examined its capability for vibration isolation and energy harvesting through static and dynamic tests. The experimental results showed that the proposed harvester achieved good vibration isolation performance at frequencies of 5 Hz and above when the magnet distance is set to 37, 39, or 41 mm. Additionally, the magnet distance significantly affected the energy harvesting performance of the harvester. Compared to the 2.144 mW output power of the configuration at a magnetic distance of 37 mm, the output power increased by 54.9% and 31.7% for the configurations with magnet distances of 41 and 39 mm, respectively. The findings suggest potential applications in precision machinery, structural vibration control, and self-powered sensing systems, where minimizing external disturbances while efficiently capturing energy is essential. Future work may focus on further optimizing the system's structural parameters and expanding its applicability to a broader range of vibration environments.

This work was financially supported by the Rolling Support Project of Outstanding Youth Science Foundation of Henan Province (Grant No. 252300421239), National Natural Science Foundation of China (Grant Nos. 52277227, 52305135, and 52307253), Program for Science & Technology Innovation Talents in Universities of Henan Province (Grant No. 23HASTIT010), the Guangdong Provincial Project (2023QN10L545), the Guangzhou Municipal Science and Technology Bureau (Grant Nos. SL2023A03J00869 and SL2023A04J01741), and Key Research & Development and Promotion Project of Henan Province (Grant No. 252102241024).

AUTHOR DECLARATIONS

Conflict of Interest

The authors have no conflicts to disclose.

Author Contributions

Junlei Wang: Conceptualization (equal); Data curation (equal); Formal analysis (equal); Investigation (equal); Methodology (equal); Software (equal); Validation (equal); Visualization (equal); Writing – original draft (equal). **Han Li:** Data curation (equal); Formal analysis (equal); Investigation (equal); Methodology (equal); Software (lead); Validation (equal); Visualization (equal); Writing – original draft (equal). **Daniil Yurchenko:** Formal analysis (equal); Investigation (equal); Methodology (equal); Supervision (equal). **Haigang Tian:** Conceptualization (equal); Formal analysis (equal); Methodology (equal); Writing – review & editing (supporting). **Guobiao Hu:** Conceptualization (equal); Funding acquisition (equal); Methodology (equal); Supervision (equal); Writing – review & editing (lead).

DATA AVAILABILITY

The data that support the findings of this study are available from the corresponding authors upon reasonable request.

REFERENCES

[1]H. Zhu, T. F. Walsh, and F. Semperlotti, Appl. Phys. Lett. **113**(22), 221903 (2018).
[2]Y. Zhang and Q. Cao, Int. J. Mech. Sci. **214**, 106904 (2022).
[3]C. Liu and K. Yu, Arch. Civ. Mech. Eng. **20**(3), 67 (2020).
[4]C. T. Lee and B. Y. Moon, Mech. Syst. Signal Proc. **20**(2), 373 (2006).
[5]S. D. Nie, Y. Zhuang, Y. Wang, and K. H. Guo, Mech. Syst. Signal Proc. **99**, 730 (2018).
[6]Ł. Konieczny, Shock Vib. **2016**(1), 6182847.
[7]T. Y. Xu, M. Liang, C. Li, and S. Yang, J. Sound Vib. **355**, 66 (2015).
[8]A. Bazinenkov and V. Mikhailov, Procedia Eng. **106**, 170 (2015).
[9]S. B. Choi, H. K. Lee, and E. G. Chang, Mechatronics **11**(3), 345 (2001).
[10]M. Valasek, M. Novak, Z. Sika, and O. Vaculin, Veh. Syst. Dyn. **27**(5–6), 289 (1997).
[11]N. A. Kamaruzaman, W. S. P. Robertson, M. H. Ghayesh, B. S. Cazzolato, and A. C. Zander, *Vibration Engineering for a Sustainable Future* (Springer, Cham, 2021), pp. 237–243.
[12]Q. Zhang, Z. Yang, C. Wang, Y. Yang, and R. Zhang, Proc. Inst. Mech. Eng., Part C **233**(11), 3804 (2019).
[13]B. Ebrahimi, H. Bolandhemmat, M. Khamesee, and F. Golnaraghi, Veh. Syst. Dyn. **49**(1–2), 311 (2011).
[14]P. Zheng, R. Wang, and J. Gao, J. Vib. Eng. Technol. **8**(1), 225 (2020).
[15]H. Tian, X. Shan, X. Li, and J. Wang, Appl. Energy **340**, 120979 (2023).
[16]B. Zhao, J. Wang, J. Liang, and W. Liao, Appl. Phys. Lett. **116**(6), 063901 (2020).
[17]K. Yang, J. Wang, and D. Yurchenko, Appl. Phys. Lett. **115**(19), 193901 (2019).
[18]H. Tian, D. Yurchenko, Z. Li, J. Guo, X. Kang, and J. Wang, Int. J. Mech. Sci. **281**, 109681 (2024).
[19]V. Annapureddy, H. Y. Lee, W. Yoon, H. Woo, J. Lee, H. Palneedi, H. Kim, J. Choi, D. Jeong, S. N. Yi, and J. Ryu, Appl. Phys. Lett. **109**(9), 093901 (2016).
[20]J. Zhou, L. He, L. Liu, G. Yu, X. Gu, and G. Cheng, Energy Convers. Manage. **258**, 115504 (2022).
[21]J. Li, G. Wang, P. Yang, Y. Wen, L. Zhang, R. Song, and C. Hou, Energy **286**, 129578 (2024).
[22]H. Chen, Q. Lu, X. Cao, N. Wang, and Z. Wang, Nano Res. **15**(3), 2505 (2022).
[23]X. Shen, X. Wang, M. Yu, H. Wang, F. Xu, and Q. Zhang, ACS Appl. Nano Mater. **7**(13), 15478 (2024).
[24]K. Tao, H. Yi, Y. Yang, H. Chang, J. Wu, L. Tang, Z. Yang, N. Wang, L. Hu, Y. Fu, J. Miao, and W. Yuan, Nano Energy **67**, 104197 (2020).
[25]Y. Tian, X. Meng, X. Lin, L. Zhang, C. Xing, H. Dai, L. Wang, Z. Peng, and B. Meng, Appl. Phys. Lett. **121**(9), 093902 (2022).
[26]K. Xu, Y. Zhang, M. Niu, and L. Chen, Mech. Syst. Signal Proc. **161**, 107956 (2021).
[27]H. Zhang, Z. Li, Z. Yang, and S. Zhou, Commun. Nonlinear Sci. Numer. Simul. **125**, 107350 (2023).
[28]S. Fang, K. Chen, Z. Lai, S. Zhou, D. Yurchenko, and W. Liao, Mech. Syst. Signal Proc. **199**, 110466 (2023).
[29]P. Banerjee, S. Dalela, P. S. Balaji, S. Murugan, and L. A. Kumaraswamidhas, Acta Mech. **234**(8), 3337 (2023).
[30]J. Kan, W. Liao, J. Wang, S. Wang, M. Yan, Y. Jiang, and Z. Zhang, Nano Energy **89**, 106466 (2021).
[31]C. Liu, R. Zhao, K. Yu, H. P. Lee, and B. Liao, Energy **233**, 121146 (2021).
[32]C. Liu, R. Zhao, K. Yu, H. P. Lee, and B. Liao, Appl. Math. Modell. **100**, 152 (2021).
[33]M. Li and X. Jing, Energy Convers. Manage. **244**, 114466 (2021).
[34]S. Fang, K. Chen, B. Zhao, Z. Lai, S. Zhou, and W. Liao, J. Sound Vib. **553**, 117684 (2023).
[35]G. Sui, X. Shan, Y. Chen, C. Zhou, C. Hou, H. Li, and T. Cheng, Energy **301**, 131711 (2024).
[36]G. Yan, J. Lu, W. Qi, F. Liu, H. Yan, L. Zhao, Z. Wu, and W. Zhang, Nonlinear Dyn. **112**(8), 5955 (2024).
[37]P. Li, N. Xu, and C. Gao, Microsyst. Technol. **26**, 1707–1716 (2020).